

Highly cross-linked carbon tube aerogels with enhanced elasticity and fatigue resistance

Received: 11 January 2023

Accepted: 9 May 2023

Published online: 01 June 2023

 Check for updatesLei Zhuang¹, De Lu¹, Jijun Zhang¹, Pengfei Guo¹, Lei Su¹, Yuanbin Qin¹, Peng Zhang¹, Liang Xu¹, Min Niu¹, Kang Peng¹ & Hongjie Wang¹✉

Carbon aerogels are elastic, mechanically robust and fatigue resistant and are known for their promising applications in the fields of soft robotics, pressure sensors etc. However, these aerogels are generally fragile and/or easily deformable, which limits their applications. Here, we report a synthesis strategy for fabricating highly compressible and fatigue-resistant aerogels by assembling interconnected carbon tubes. The carbon tube aerogels demonstrate near-zero Poisson's ratio, exhibit a maximum strength over 20 MPa and a completely recoverable strain up to 99%. They show high fatigue resistance (less than 1.5% permanent degradation after 1000 cycles at 99% strain) and are thermally stable up to 2500 °C in an Ar atmosphere. Additionally, they possess tunable conductivity and electromagnetic shielding. The combined mechanical and multi-functional properties offer an attractive material for the use in harsh environments.

Carbon aerogels (CAs) demonstrating high mechanical strength, compressive resilience, and fatigue resistance are fitting harsh environments in the industries such as heat sealing, energy dissipation, pressure sensors, and aerospace vehicles^{1–3}. However, achieving these properties in a material is a critical challenge due to their mutually exclusive nature^{4,5}, which severely restricts the CAs' applications. Constructing robust, elastic and fatigue-resistant CAs with controllable architectures, are highly promising^{6,7}.

Traditional CAs, made from activated or non-graphitizable carbons, have limited deformability and are fragile⁸. There have been recent advancements in constructing CAs using flexible nano-units such as one-dimensional carbon fibers and two-dimensional graphene as structural components. By assembling these nano-units into three-dimensional porous architectures, CAs with elasticity can be realized^{9–11}. The porous architectures comprising large voids facilitate the deformation of elastic struts within them. Nonetheless, the facile deformation of these struts results in relatively low mechanical strength of the corresponding CAs. For instance, carbon fiber-assembled CAs can be compressed up to 90% strain (ϵ), but their tested strength may not surpass 65 kPa¹². Besides, CAs typically exhibit permanent deformation and strength loss after cyclic compression

(e.g., -17.3% strength loss after 100 cycles at $\epsilon = 90\%$ ¹³). So far, the goals of high mechanical strength and good recoverable cyclic compressibility with minimal structural degradation have not been accomplished for CAs yet.

Biological networks, such as cobweb and bacterial cellulose made of fibrous proteins, have evolved to fulfill multiple functions, including efficient storage and dissipation of energy. Their cross-linked architectures make them one of the strongest and toughest materials with deformability ever known¹⁴. For such materials, force tends to transfer fast along the struct and to many others through junctions during deformation. Thus, to improve the mechanical strength and elasticity of materials, cross-links between the structs need to be rationally designed^{15–18}. Polyacrylamide-based hydrogels are a typical example of cross-linked architectures that possess enhanced mechanical properties. They exhibit a maximum compressive stress over 90 kPa and their residual deformation is mere 6% after 500 cycles at $\epsilon = 70\%$ ¹⁹. Despite much effort, researchers are still facing challenges in precisely controlling the cross-links of these materials, and so achieving the desired mechanical performance.

Apart from the design of micro-architectures, the characteristics of struts play a crucial role in determining the compressive behaviors

¹State Key Laboratory for Mechanical Behavior of Materials Xi'an Jiaotong University, 710049 Xi'an, China. ✉e-mail: hjwang@xjtu.edu.cn

of CAs^{20,21}. Multi-wall carbon tubes are considered one of the most suitable struts for constructing robust aerogels due to their exceptional mechanical properties. In particular, carbon tubes demonstrate high flexibility and can adapt and switch when buckling, enabling them to endure local strain while preserving their structural integrity²². This makes them an ideal candidate for creating high-performance CAs. Although carbon tubes have an ultra-high theoretical tensile strength reaching ~100 GPa²³, their bending and buckling strength is generally limited due to weak interwall van der Waals coupling that causes easy sliding between walls²⁴. This results in near-zero friction and small energy dissipation²⁵, but also leads to unsatisfactory mechanical strength of corresponding aerogels.

Here, we demonstrate an approach to fabricating high-performance carbon tube aerogels (CTAs) that possess a highly cross-linked architecture. The carbon tubes, which feature sp^2 and sp^3 hybridization, exhibit improved stiffness and strength. Owing to the high cross-links and robust constituents, CTAs with a low density show enhanced mechanical properties, including a maximum compressive stress of 20.9 MPa and a completely recoverable strain up to 99%. Additionally, the CTAs we prepared demonstrate high fatigue resistance, with almost negligible permanent deformation (<1.5%) and strength loss (<2%) at $\varepsilon = 99\%$ for 1000 compressive cycles. These results are among the best reported elastic materials. Moreover, they are thermally stable in an Ar atmosphere at a temperature as high as 2500 °C. As a result, we believe that they present great potential for use in a variety of practical applications, such as high-precision pressure sensors designed to operate in severe environments.

Results

Fabrication and structural characterization

We employed a simple yet effective approach that combines sacrificial template and chemical vapor deposition (CVD) to prepare CTAs. Typically, conventional macroscopic aerogels constructed from nanowires or nanofibers have low densities (less than 50 mg cm⁻³), which results in insufficient connections between the constituents and minimal constituent content²⁶. To overcome this challenge and synthesize macroscopic CTAs with strong cross-links, we utilized silicon carbide (SiC) nanowire aerogels as raw materials²⁷. The initial density of these aerogels is also low, ranging from 10 to 20 mg cm⁻³, as demonstrated in Supplementary Fig. 1a; however, their density can be enhanced by subjecting them to hot-pressing. The initial aerogels that possess a highly porous isotropic architecture, are assembled by nanowires in diameters ranging from 90–160 nm, as demonstrated in Supplementary Fig. 2. Upon subjecting these raw aerogels to hot-pressing conditions (1200 °C for 2 h in Ar, at a pressure of 10–15 MPa), a laminar structure with significantly higher density of nanowires (200–300 mg cm⁻³) was obtained (see Supplementary Figs. 1b and 3). The wave-like morphology observed in the laminar aerogels is hypothesized to result from uneven stress distribution during hot-pressing²⁸. The presence of space between the thin lamellas may facilitate deformation of the flexible constituents upon compression. To connect the nanowires, the hot-pressed aerogels were then exposed to oxidation in a furnace at 1000 °C for 24 h in air, resulting in the transformation of SiC to SiO₂. This transformation also aided in the subsequent removal of ceramic nanowires through acid corrosion²⁹. The laminar SiO₂ aerogels, obtained with a sufficient number of nanowires and cross-links, served as an ideal template for the deposition. A core-shell structure was formed when coating the laminar SiO₂ nanowire aerogels with carbon layers. Upon removal of the SiO₂ cores using hydrofluoric acid, lightweight, highly cross-linked CTAs were ultimately acquired, as shown in Fig. 1a.

The CTAs, inheriting the architecture of raw laminar nanowire aerogels, exhibit a multitude of cross-links, as illustrated in Fig. 1b, c. The hollow structure of the carbon constituents is verified by transmission electron microscope (TEM) imaging and corresponding

energy dispersive spectroscopy (EDS) mapping analysis in Fig. 1d, imparting an ultralight characteristic to the CTAs (refer to Supplementary Fig. 4, where the density of CTAs was as low as 12.5 mg cm⁻³). Most synthesized carbon tubes resemble seamless, rolled graphene, with in-plane atoms bonded through localized sp^2 hybridization. But both theoretically and experimentally, it is proven that the concentration of defects, such as stacking faults and shearing of lattice planes, as well as the distribution of local strain, can initiate low-energy transformation windows, thereby triggering the thermodynamics of sp^2 -to- sp^3 phase transition³⁰. In fact, the growth of single-crystal graphene is heavily influenced by the surface conditions of template³¹. Carbon atoms are energetically favorable on top of the first-layer template based on the lowest-energy principle. In the case of our SiO₂ nanowire templates, numerous step edges are present on their surface. Consequently, during deposition, when graphene sheets grow and subsequently encounter, the formation of defects such as stacking faults and shearing of lattice planes occurs, as depicted in Fig. 1e. The encountered regions enduring dramatic compressive strain, may lead to a reduction in C-C interatomic and interwall distance, therefore prompting the atomic rearrangements of carbon atoms from sp^2 to sp^3 and positioning them in the most favorable locations. This is corroborated by Raman and X-ray photoelectron spectroscopy (XPS) analyses which reveal the presence of both sp^2 and sp^3 in the tubes (Fig. 1f, g).

It is noteworthy that, these sp^2 and sp^3 of carbon systems correspond to very defined orbital states³². sp^2 is the hybridization of the atomic 2s orbital with $2p_x$ and $2p_y$ orbitals, resulting in a system of three planar σ -bonds forming an angle of 120°. The remaining $2p_z$ orbital that is perpendicular to the plane of the σ -bonds, forms a π -bond. sp^3 corresponds to the hybridization of the atomic 2s orbital with its three $2p_x$, $2p_y$, and $2p_z$ orbitals in equal proportion, leading to the creation of a tetrahedral σ -bond system at an angle of 109.5°³³. The bonding states are accompanied by unoccupied anti-bonding states σ^* and π^* . The electron energy loss spectroscopy (EELS) mapping in Fig. 1h shows that the π^* fraction varies between 0.32 to 0.45, suggesting that the distribution of π^* and σ^* bands is approximately uniform along the tube (typical curves of C-K spectra are given in Supplementary Fig. 5). This observation also demonstrates that the tube walls exhibit a homogeneous blend of sp^2 and sp^3 bonds.

The joints between carbon tubes were analyzed by TEM and EELS, as presented in Supplementary Fig. 6. The TEM image (Supplementary Fig. 6a–c) reveals a welded joint between the two tubes, with an overlapped regime. This structure is speculated to result from the drop height between the original SiO₂ nanowire templates. As illustrated in Supplementary Fig. 6d, the growth of carbon layers on the templates attributes to the formation of bonds between atoms in the same plane, while the remaining parts of the carbon layers continue to grow along the templates, resulting in a cross joint between the tubes. Upon treated by acid corrosion, through EELS spectra (Supplementary Fig. 6e), it is validated that the SiO₂ templates have been removed all, leaving no Si element in the tubes. The well-connected structures observed in the CTAs may be a key determinant of their mechanical properties.

Mechanical properties

The mechanical properties of the CTAs are shown in Fig. 2a. The typical stress vs. strain curves exhibit three characteristic deformation regions: a nearly linear elastic regime for $\varepsilon \leq 5\%$; a subsequent plateau regime for $5\% < \varepsilon \leq 80\%$; and a sharply increasing stress regime for $\varepsilon \geq 80\%$. Clearly, the fully recoverable strain of our CTAs (with a density of 12.9 mg cm⁻³), can be up to $\varepsilon = 99\%$ (see the inset zoom-up curve in Fig. 2a), corresponding to an ultimately compressive stress of 8.2 MPa. The density of CTAs can be further tuned to ~20–40 mg cm⁻³ by adjusting the CVD time to ~140–280 min. The prepared CTAs with the highest density of 43.2 mg cm⁻³, can withstand a maximum stress of

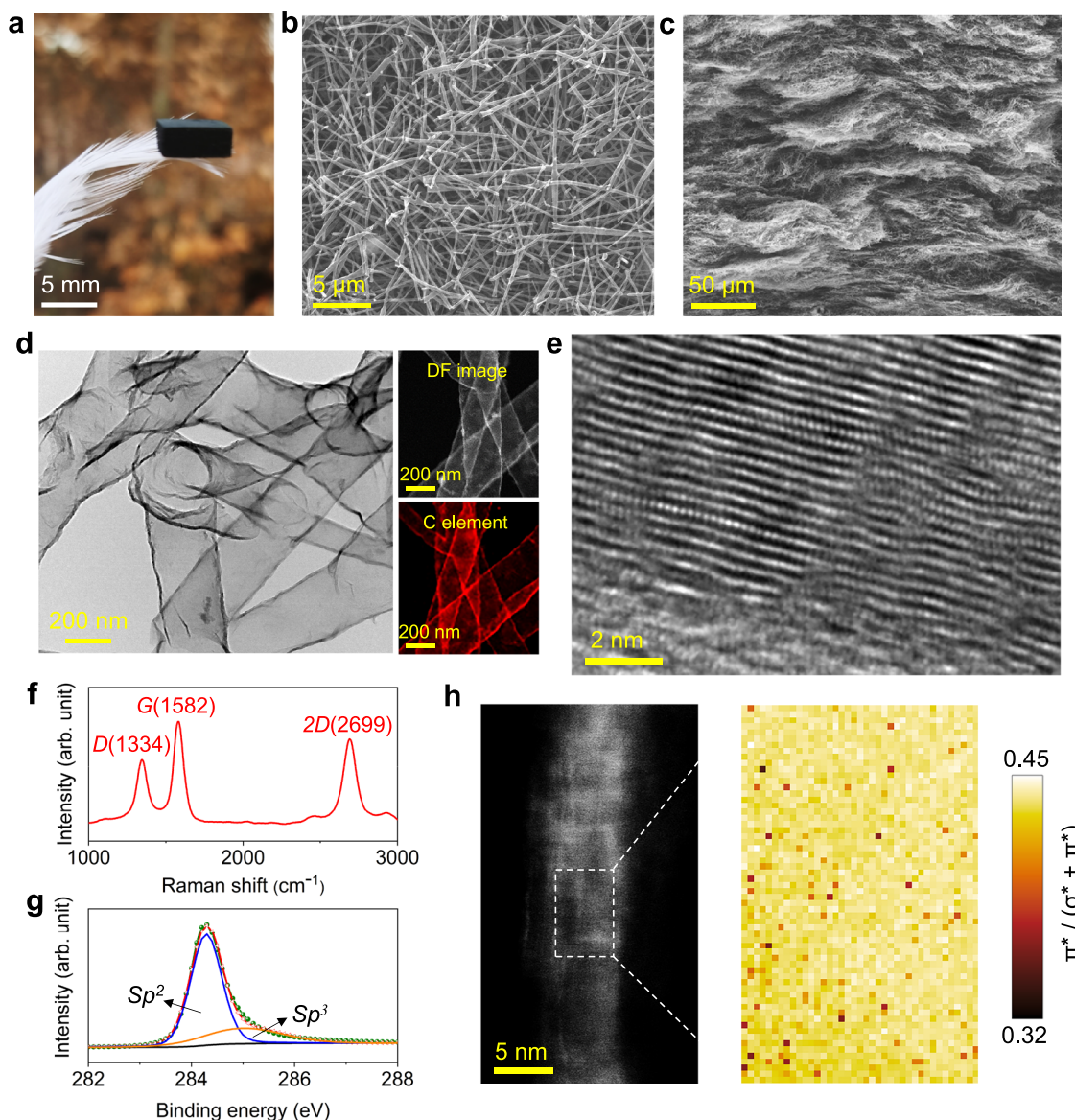


Fig. 1 | Structure of carbon tube aerogels (CTAs). **a** Lightweight characteristic of a CTA that stands on a feather. **b** Surface scanning electron microscope (SEM) image of CTAs. **c** Cross-section SEM image of CTAs. **d** Transmission electron microscope (TEM) image of the carbon tube network in CTAs. The right top and right bottom images are dark field (DF) TEM and energy dispersive spectroscopy (EDS) mapping of carbon tubes, respectively. **e** Typical high-resolution TEM of the wall of a carbon

tube. **f** Raman spectrum of CTAs, showing three typical characteristic peaks of *D*, *G*, and *2D*. **g** X-ray photoelectron spectroscopy (XPS) spectrum of CTAs, showing that two types of bonds are present in the tubes. **h** Electron energy loss spectroscopy (EELS) mapping of a carbon tube wall, showing the ratio of π^* to $(\sigma^* + \pi^*)$ using two-window intensity-ratio method³². Source data are provided as a Source Data file.

20.9 MPa at $\epsilon = 98\%$, and show mechanically recoverable behaviors with no permanent deformation as well, as presented in Supplementary Fig. 7. The architecture of highly cross-linked carbon tubes, characterized by abundant joints, enables rapid load transfer and homogenous stress distribution, leading to the good mechanical properties of CTAs.

However, excessively high cross-links (using $\sim 300 \text{ mg cm}^{-3}$ nanowire aerogels as template, as shown in Supplementary Fig. 8) can result in an obvious decrease in the recoverability of CTAs, despite an increase in compressive stress. This is due to the fact that the closer junctions shorten the length-to-diameter (L/D) ratio of carbon tubes, which improves the stress modulus of the tubes but also, increases their curvature when bending, ultimately reaching their maximum critical limits.

Experimental snapshots of cross-sectional views (Fig. 2b, captured from Supplementary Movie 1) and in situ SEM observations during

uniaxial compression (Fig. 2c) both confirm that CTAs exhibit a near-zero Poisson's ratio. This characteristic can restrict local indirect tension, reducing permanent deformation and enhancing dimensional stability during compression.

We proceeded to assess the fatigue resistance of our CTAs. Through cyclic testing (Fig. 2d and Supplementary Fig. 9), we observe that the 100th and 1000th loops of CTAs remain nearly unchanged in comparison to the 1st cycle, displaying a maximum stress retention of up to 97.9% (8.19 MPa for the 1st cycle, and 8.02 MPa for the 1000th cycle) and a residual strain of less than 1.5% at $\epsilon = 99\%$. The energy loss coefficient for the 1st cycle is 0.338, indicating that energy dissipation can occur by interfacial slipping between the carbon tubes during compression. After 1000 cycles, energy loss coefficient of the CTAs slightly decreases to 0.332 (Fig. 2e), demonstrating that almost no significant damage or structural collapse happens during cyclic compression. Our CTAs, possessing high mechanical strength,

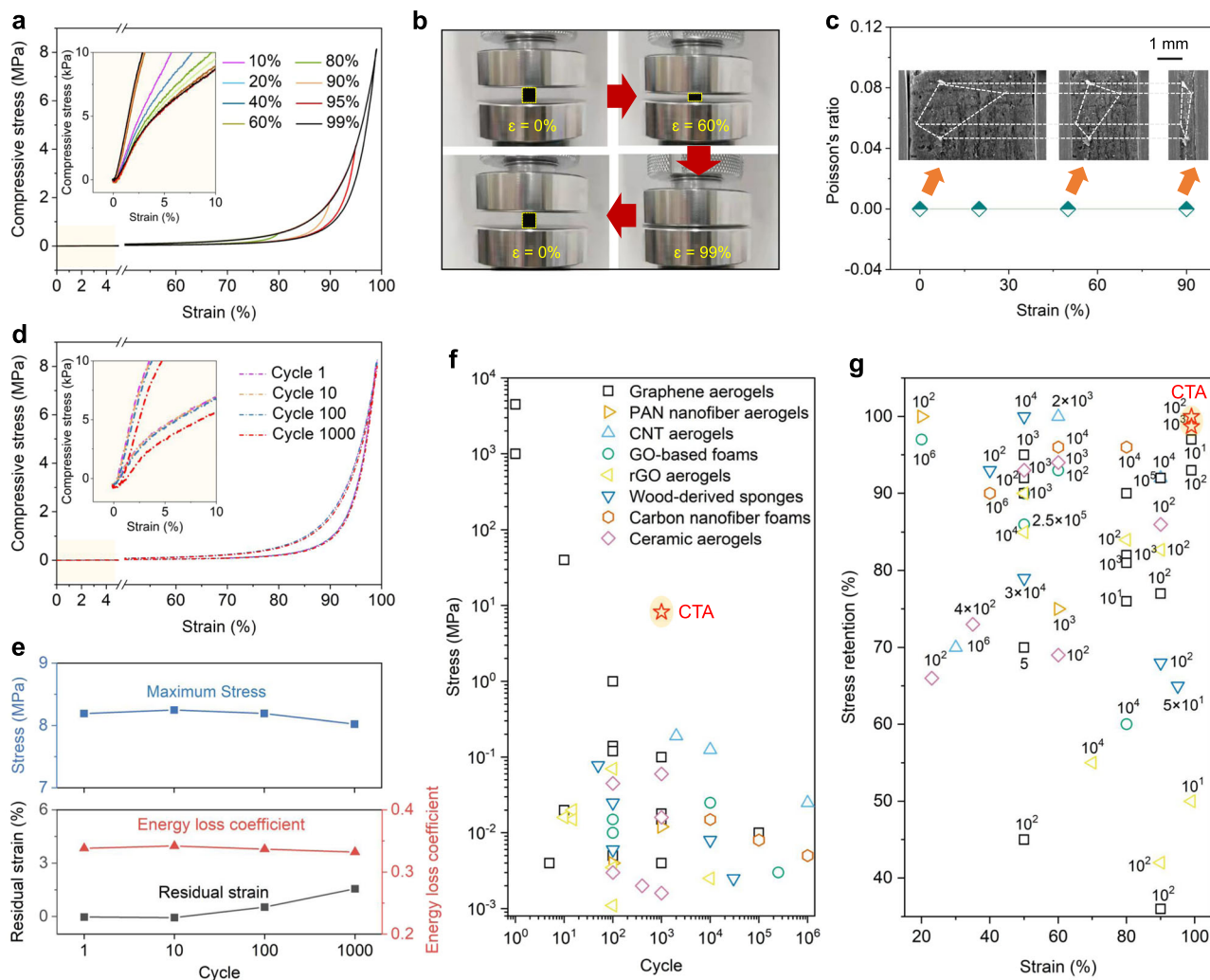


Fig. 2 | Mechanical properties of carbon tube aerogels (CTAs). **a** Stress vs. strain curves of a CTA (12.9 mg cm^{-3}) compressed to 10–99% strain. Inset: Enlarging the onset of the compression curves, demonstrating no permanent deformation. **b** Experimental snapshots of a CTA ($7 \text{ mm} \times 7 \text{ mm} \times 8 \text{ mm}$) under uniaxial compression to 99% strain. **c** Poisson's ratio of a CTA at different compressive strain (0–90%). Inset: Corresponding in situ scanning electron microscope (SEM) observations, showing a near-zero Poisson's ratio of the CTA. **d** Compressive stress vs. strain curves of a CTA at 99% strain for 1000 cycles. Inset: Enlarging the onset of the cyclic curves, showing that there is 1.5% residual deformation after 1000 cycles.

e Residual strain, stress, and energy loss coefficient of CTAs for different compressive cycles. **f** Stress vs. cycle of CTAs compared to other elastic materials such as graphene aerogels^{7–9,17,34–40}, graphene oxide (GO)-based foams^{10,11,41}, polyacrylonitrile (PAN) and carbon nanofiber aerogels^{12,42}, wood-derived carbon sponges^{43–45}, carbon nanotube (CNT) aerogels^{5,16}, reduced graphene oxide (rGO) aerogels^{13,46,47}, and ceramic aerogels^{18,40,48–52}. **g** Stress retention vs. strain of CTAs during cycles compared to previously reported materials^{5,7–13,16–18,34–52}. The cycles are marked next to the symbols. Detailed information is available in Supplementary Table 1. Source data are provided as a Source Data file.

compressive resilience, and fatigue resistance, are one of the most elastic and durable, compared to other materials^{5,7–13,16–18,34–52}, as exhibited in Fig. 2f, g.

To investigate the thermal stability of CTAs, we subjected them to annealing at $2500 \text{ }^\circ\text{C}$ for 12 h in an Ar atmosphere. All samples remain structurally intact with no visible changes. We selected the CTA with the highest density of 43.2 mg cm^{-3} for further analysis. The original sample exhibits a compressive stress of 20.9 MPa at a recoverable strain of 98%, as shown in Supplementary Fig. 10a. Whereas after annealing, the compressive stress of the sample under the same testing conditions reduces to 11.9 MPa (see Supplementary Fig. 10b); however, interestingly, its elasticity appears to have slight improvement, as evident from a comparison of the curves in Supplementary Fig. 10c, d. Additionally, Supplementary Fig. 10e demonstrates that the annealed CTA presents a higher energy loss coefficient (an increase of 0.45–1 based on different strain), indicating an enhanced ability to absorb energy.

As presented in Supplementary Fig. 11, the disorder-induced D band (-1334 cm^{-1}) in CTAs weakens noticeably after $2500 \text{ }^\circ\text{C}$ annealing,

while the first-order graphite G band (-1582 cm^{-1}) becomes sharp and strong. This suggests a marked increase in intrinsic structural sp^2 order. The possible reason is that the ultra-high temperature annealing triggers sp^3 -to- sp^2 phase transition, causing carbon atoms to rearrange into a purely sp^2 -graphite structure owing to their high activity at $2500 \text{ }^\circ\text{C}$. Our experimental results indicate that sp^3 may be one of the key factors to strengthen the carbon tubes, contributing to the improved mechanical properties of CTAs, particularly their stress values.

Mechanism understanding of mechanical properties

To gain insight into the reversible compression mechanism of CTAs, we utilized in situ TEM to observe the structural evolution during the pressing and releasing process. As shown in Fig. 3a and Supplementary Movie 2, the tubes near the indenter initially move in the direction of uniaxial compression. With an increase in indentation depth, the loading force transfers to adjacent carbon tubes through joints, resulting in a larger range of carbon tubes deforming. This

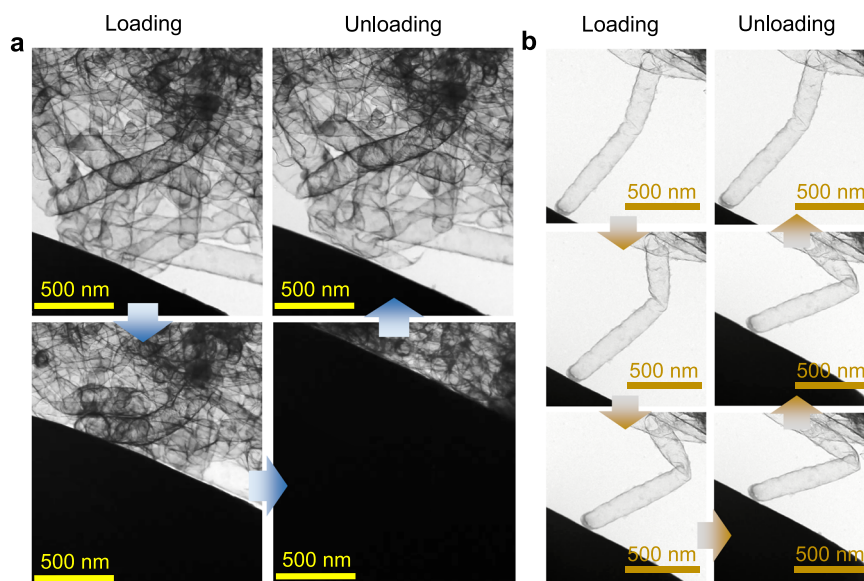


Fig. 3 | Compressive mechanism of carbon tube aerogels (CTAs). **a** In situ Transmission electron microscope (TEM) observations of carbon tube networks during uniaxial loading and unloading. **b** In situ TEM observations of a single carbon tube during bending.

phenomenon impedes local stress concentration and permanent damage, as the tubes can move to the most appropriate positions. This interpretation also explains the high mechanical values of CTAs, as presented in Fig. 2f, g. In situ TEM observations of a single tube (Fig. 3b and Supplementary Movie 3) confirm bending, rotating, and distorting of the carbon tube during compression. Upon release of the load, the compressed carbon tube springs back to its original shape, demonstrating good elasticity and flexibility.

To achieve deeper understanding of the atomic bending behaviors of carbon tubes, we carried out molecular dynamic (MD) analyses using Large-scale Atomic/Molecular Massively Parallel Simulator (LAMMPS) software⁵³. It is well-known that the walls of purely sp^2 carbon tubes, where in-plane atoms are bonded through localized sp^2 hybridization, are connected by van der Waals forces between walls. As the tube bends, these weak interactions allow for relative motions such as wrinkling, sliding, and separating of the walls, as illustrated in Fig. 4a. Although these localized motions help prevent the breakage of sp^2 bonds (with a low breakage fraction of sp^2 bonds, at only 2.2%), they have a negative impact on the bending stability and overall strength of the tube.

When we introduced 5% sp^3 and established interwall coupling, as depicted in Fig. 4b, the shortened interwall distance and the pinning effect of sp^3 bonds between walls restrict the wall movements, resulting in minimal wrinkling in the sp^2 - sp^3 hybrid tube. This improves the stiffness and strength of the tube, as demonstrated in Fig. 4c. Nevertheless, during bending of the tube, some sp^3 bonds may reach their maximum critical limits and separate (40.8% sp^3 in the present model, as shown in Fig. 4d). The breakage of these localized sp^3 bonds allows sp^2 walls to move freely again (see Fig. 4e and Supplementary Movie 4). Overall, the partial fracture of sp^3 bonds may not affect the elasticity of carbon tubes due to the majority of remaining sp^2 bonds.

Dynamic mechanical and electromagnetic performance

We conducted impact resistance tests on CTAs by dropping a steel ball that was ~200 times heavier than the samples. To capture the falling and rebounding process, we utilized a high-speed camera. As shown in Fig. 5a, when the ball hits the CTA surface at a velocity of 2083 mm s^{-1} , the sample undergoes significant deformation but quickly recovers without any structural damage or collapse. The rebound velocity of the ball is 847 mm s^{-1} . To calculate the impact and rebound energies, we used the formulas $E_i = mv_i^2/2$ and $E_r = mv_r^2/2$, where m represents the

mass of the steel ball, v_i is the impact velocity, and v_r is the rebound velocity. The result shows that CTAs can dissipate 83.4% energy during impact testing, demonstrating that they may serve as a damping material.

We performed a thorough investigation into the viscoelastic properties of CTAs, utilizing a dynamic mechanical analysis (DMA) to analyze their storage modulus, loss modulus, and damping ratio. Figure 5b illustrates that CTAs present a rapid and precise dynamic response across a wide frequency range (0.1–150 Hz). The damping ratio remains consistent at an average of 0.25 throughout the tests, regardless of frequency. Moreover, CTAs display stable thermo-mechanical performance in air conditions within a broad temperature range of -120 to 300 °C. To assess their fatigue resistance, we subjected CTAs to 100,000 cycles at oscillatory $\varepsilon = 10\%$. The dynamic mechanical values for the 1st and 100,000th cycles show negligible changes, indicating that CTAs possess temperature-invariant elasticity and fatigue-resistant properties.

As CTAs are compressed, the carbon tubes come into close proximity, creating conductive channels that can increase their conductivity. For example, when the compressive strain reaches 95%, the σ of CTAs jumps from 0.12 to 111.69 S cm^{-1} , demonstrating a wide tuning range, as shown in Supplementary Fig. 12.

It is worth mentioning that, σ has a dramatic impact on the electromagnetic interference (EMI) shielding effectiveness (SE) of materials⁵³. In this study, uncompressed CTAs in a low conductive state exhibit a reflection shielding effectiveness (SE_R) and an absorption shielding effectiveness (SE_A) of -7 dB and -8 dB, respectively, leading to a total shielding effectiveness (SE_T) of -15 dB, as depicted in Fig. 5c.

Upon compressing the CTAs to $\varepsilon = 50\%$, a noticeable increase in SE_T to -45 dB is achieved. The proposed shielding mechanism of the compressed CTAs is illustrated in Fig. 5d. As subjected to compression, the carbon tubes are compelled to come into close contact, thereby facilitating the establishment of efficient electron transport channels. This enhances the migration and hopping of electrons. In addition, the laminar architecture of CTAs gives rise to the occurrence of multiple interfacial reflections, which enables electromagnetic waves to be reflected between the carbon tube layers until they are completely absorbed and dissipated as heat. For our laminar CTAs with a 2-mm thickness, numerous carbon tube layers can serve as effective barriers to electromagnetic waves, resulting in little transmission of waves through the CTAs.

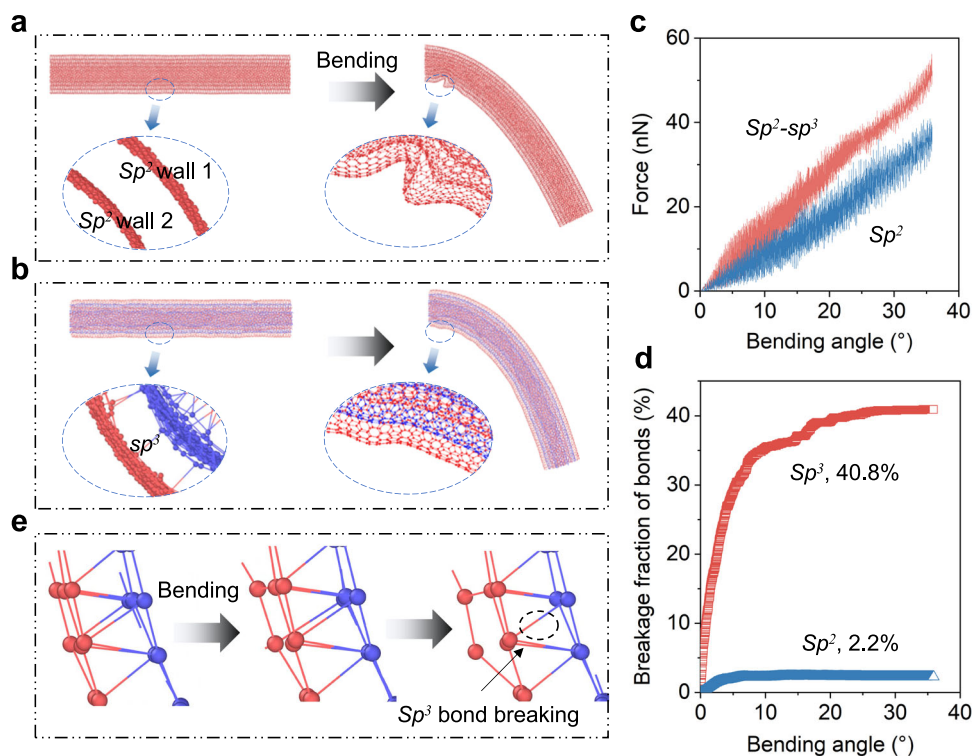


Fig. 4 | Molecular dynamic (MD) simulation of five-layer carbon tubes during bending (simulated using LAMMPS software). **a** The tube with purely sp^2 bonds. **b** The tube with sp^2 - sp^3 hybrid bonds. **c** The force vs. bending angle curves of two

types of carbon tubes during bending. **d** The breakage fraction of sp^2 and sp^3 bonds during bending. **e** Breaking process of sp^3 bonds during bending of a sp^2 - sp^3 hybrid tube. Source data are provided as a Source Data file.

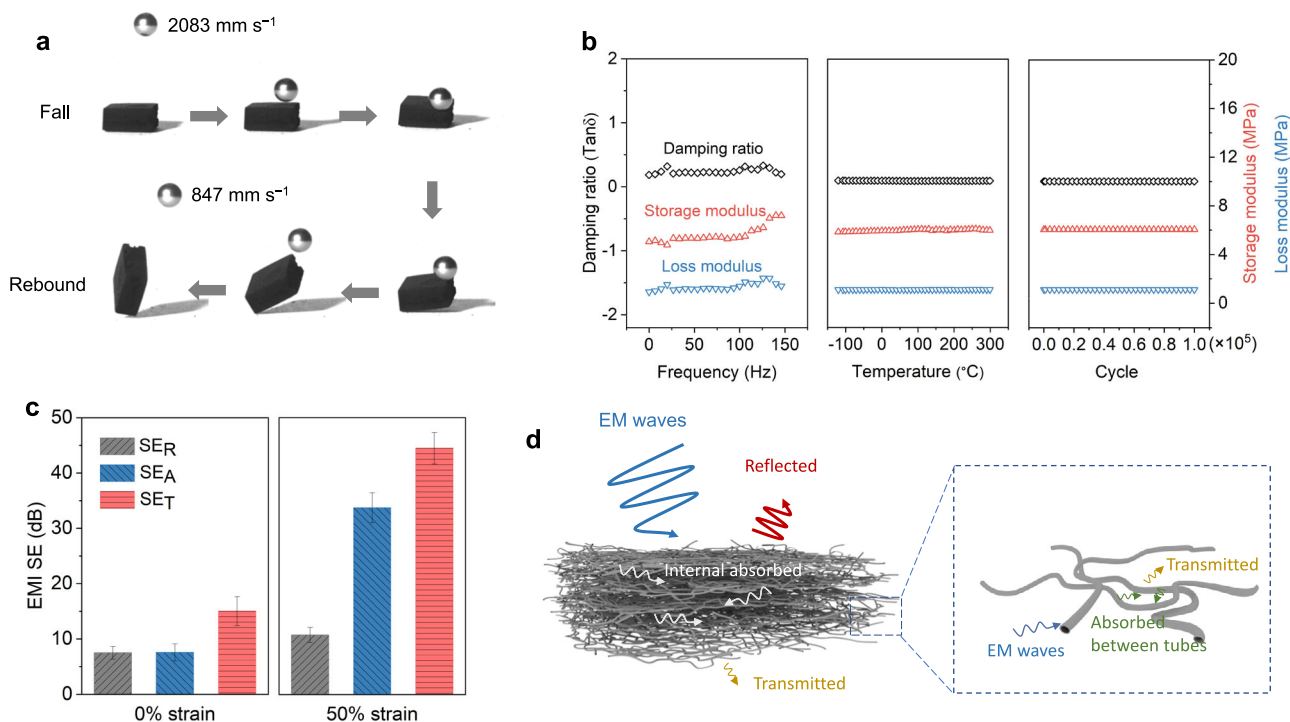


Fig. 5 | Dynamic mechanical properties and electromagnetic interference (EMI) shielding performance of carbon tube aerogels (CTAs). **a** Impact resistance of a CTA tested by dropping a free-falling steel ball. **b** Damping ratio, storage modulus, and loss modulus of CTAs measured by a dynamic mechanical analysis (DMA) at different frequencies, temperatures and compressive cycles. **c** EMI shielding effectiveness (SE) of CTAs at 0 and 50% strain. The reflection shielding effectiveness

(SE_R), absorption shielding effectiveness (SE_A), and total shielding effectiveness (SE_T) for 5% compression are 7.48 ± 1.14 , 7.54 ± 1.55 , and 15.02 ± 2.61 dB, respectively, and are 10.75 ± 1.37 , 33.73 ± 2.71 , and 44.48 ± 2.85 dB, respectively, for 50% compression. **d** Schematic diagram of shielding mechanism of CTAs. Source data are provided as a Source Data file.

Discussion

An effective approach was presented to fabricate high-performance CTAs. The highly interconnected carbon tubes with sp^2 - sp^3 hybrid bonds enable rapid load transfer. As a result, the CTAs with a low density (~ 12 – 40 mg cm^{-3}) demonstrate good mechanical properties, including high mechanical strength (8.2–20.9 MPa), compressive resilience (up to 99% strain), and fatigue resistance (less than 1.5% permanent deformation after 1000 compressive cycles at 99% strain). Moreover, the CTAs possess high thermal stability up to 2500 °C in an Ar atmosphere.

Our CTAs exhibit promising potential as a viable candidate for various applications, such as impact resistance and energy dissipation, mainly since they can absorb up to 83.4% impact energy without incurring any structural damage, as demonstrated through free-falling steel ball testing. Furthermore, their high elasticity allows for adjustable electrical conductivity and tunable electromagnetic shielding behaviors. These properties make them ideal for use such as in wearable electronics, and high-precision pressure sensors.

Methods

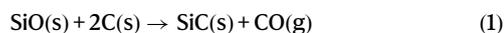
Raw materials and chemicals

Methyltrimethoxysilane (MTMS, analytical reagent, 99.8%), dimethyldimethoxysilane (DMDMS, analytical reagent, 99.7%), deionized water (analytical reagent, 99%), and hydrofluoric acid (guaranteed reagent, 40%) were purchased from Meryer Technologies Co., Ltd. Please note that, it is extremely important to be fully aware of safety and emergency protocols when working with hydrofluoric acid. Ethanol (analytical reagent, 99.5%) was purchased from Sinopharm Chemical Reagents Co., Ltd. Short carbon fibers (powders, 99%) were purchased from Guangwei Composites Co., Ltd. Hydrogen (H_2 , 99.999%), argon (Ar, 99.999%), and methane (CH_4 , 99.999%) gases were purchased from Xi'an Jiayihe Gas Co., Ltd. All chemicals were used in their as-received conditions without further purification.

Synthesis of SiC nanowire aerogels

MTMS (40 g), DMDMS (10 g), ethanol (100 g), and deionized water (60 g) were mixed by mechanical stirring for 30 min to form an ethanol solution of siloxane sol²⁷. The hydrolysis of $-\text{Si}-\text{OCH}_3$ group from MTMS and DMDMS, results in the formation of $-\text{Si}-\text{OH}$, while the polycondensation between $-\text{Si}-\text{OH}$ groups leads to the formation of siloxane sol. Short carbon fibers (20 g) were put and dispersed in the siloxane sol by mechanical agitation for 20–30 min to form a mixture solution.

The mixture solution was subjected to vacuum filtration to remove the liquids, and the carbon fiber skeletons with viscous siloxane sol left in the pores were obtained. The skeletons were then treated at 100 °C in an oven for 5 h. Subsequently, the skeletons with siloxane gel were heated to 1550 °C at a rate of 5 °C min^{-1} in an Ar atmosphere and a constant pressure of 0.2 MPa. After holding for 2 h in this condition, entangled SiC nanowires were formed inside the skeletons according to the following reactions:



The obtained skeletons were treated at 700 °C in air for 3 h to remove the carbon fibers. Finally, high-purity SiC nanowire aerogels with a density of 10 – 20 mg cm^{-3} were acquired. The yield of isolated mass for SiC nanowire aerogels (the mass ratio of nanowires to siloxane sol) were calculated to be $\sim 40\%$.

Synthesis of laminar SiO_2 nanowire aerogels

Hot-pressing (1200 °C for 2 h) was applied on the raw SiC nanowire aerogels to increase their density. The pressure was set to be 10 – 15 MPa according to the desired density of nanowires (200 – 300 mg cm^{-3}). During the hot-pressing process, a laminar structure naturally forms in the aerogels. Then, these aerogels were subjected to 1000 °C in a furnace for 24 h to fully oxidize SiC into SiO_2 . As a result, laminar SiO_2 nanowire aerogels were obtained.

Synthesis of CTAs

The SiO_2 laminar nanowire aerogels were to deposit carbon layers by CVD. The CVD temperature was set to be 1190 °C, and CH_4 (20 ml min^{-1}), H_2 (50 ml min^{-1}), and Ar (200 ml min^{-1}) were used as reactive gas, purify gas and dilute gas, respectively. The deposition time was 70–280 min according to the final density of CTAs (~ 12 – 40 mg cm^{-3}).

The SiO_2 nanowire cores were completely etched by hydrofluoric acid for 6 h at 60 °C in air conditions, followed by washing with deionized water for several times. When handling hazardous hydrofluoric acid, independent of the concentrations, it is critical to be aware of the risk assessment and requires safety protocols. The wet CTAs were naturally dried for 24 h, and ultimately hollow CTAs (with a density of ~ 12 – 40 mg cm^{-3}) were acquired.

Material characterization

The microstructure evolution of CTAs was investigated using in situ SEM (Quanta 600, FEI, United States) operated at an acceleration voltage of 200 kV, and in situ TEM (JEM-2100, JEOL, Japan) equipped with EDS at an acceleration voltage of 200 kV. The elemental and structural analyses were carried out by XPS (ESCALAB Xi+, Thermo Fisher, United States), Raman (InVia Qontor, Renishaw, United States) with a 532-nm laser, and aberration-corrected TEM (HF5000, Hitachi, Japan) at an acceleration voltage of 100 kV equipped with EELS. The band ratio of π^* to ($\sigma^* + \pi^*$) was determined by integrating the π^* peak (I_π) and the remaining area starting at the σ^* edge (I_σ) using a two-window method³². The compressive properties of CTAs were investigated via a universal tester (UTM2103, Suns Co., Ltd., China) with a 1000 N load cell. The loading and unloading rates were 5 mm min^{-1} . The viscoelastic properties of CTAs were studied using DMA (DMA242E, Netzsch, Germany). At least 5 samples were tested for each condition, and no data were excluded from the analyses.

EMI shielding tests were performed on a vector network analyzer (E5071C, Rohde & Schwarz, Germany). The samples were cut into a cuboid shape ($22.84 \text{ mm} \times 10.14 \text{ mm} \times 2 \text{ mm}$). The SE_R and SE_A were expressed as⁵⁴:

$$\text{SE}_R = 20 \log \left(\frac{\sqrt{u_0 \epsilon_0}}{4 \sqrt{2\pi f u}} \right) \quad (3)$$

$$\text{SE}_A = 8.686 d \sqrt{\pi f u_0} \quad (4)$$

where f is the testing frequency, u is the magnetic permeability of a material, u_0 and ϵ_0 are the permeability and permittivity of free space, respectively, and d is the thickness of a material.

Experimentally, SE_R and SE_A were measured in terms of reflection and effective absorption, considering the power of the incident electromagnetic waves inside a shielding material as⁵⁵:

$$\text{SE}_R = 10 \log \left(\frac{1}{1 - |\text{S11}|^2} \right) \quad (5)$$

$$\text{SE}_A = 10 \log \left(\frac{1 - |\text{S11}|^2}{|\text{S21}|^2} \right) \quad (6)$$

where S_{11} and S_{21} are the scattering parameters given by the vector network analyzer directly. The SE_T was given as:

$$SE_T = SE_R + SE_A \quad (7)$$

At least 3 samples were tested for EMI shielding tests, and no data were excluded from the analyses. The data presented in the article were the mean values of all samples.

Computational simulations

LAMMPS software was utilized to conduct MD simulations on carbon tubes. The five-layer tubes were constructed at a L/D ratio of 6.2. To create the sp^2 - sp^3 hybrid tube, 5% sp^3 was set to be randomly distributed among the remaining 95% sp^2 bonds. The purely sp^2 tube was created by utilizing exclusively sp^2 bonds. Upon bending, a curvature of 35.9° was given. In general, the bond lengths of sp^2 and sp^3 in carbon atoms fell within the range of 0.13–0.15 and 0.15–0.17 nm, respectively^{56–58}. Therefore, we defined when sp^2 and sp^3 bonds exceeded 0.16 and 0.18 nm, respectively, they were considered broken. The visualization of carbon tube models was conducted using OVITO⁵⁹.

Data availability

The data that supports the findings of this study are available in the article and supplementary information file. Source data are provided with this manuscript. Source data are provided with this paper.

References

1. Yeo, S. J., Oh, M. J. & Yoo, P. J. Structurally controlled cellular architectures for high-performance ultra-lightweight materials. *Adv. Mater.* **31**, 1803670 (2019).
2. Zhao, K. et al. Super-elasticity of three-dimensionally cross-linked graphene materials all the way to deep cryogenic temperatures. *Sci. Adv.* **5**, eaav2589 (2019).
3. Suhr, J. et al. Fatigue resistance of aligned carbon nanotube arrays under cyclic compression. *Nat. Nanotechnol.* **2**, 417 (2007).
4. Zheng, X. et al. Ultralight, ultrastiff mechanical metamaterials. *Science* **344**, 1373–1377 (2014).
5. Kyu, H. K., Youngseok, O. & Islam, M. F. Graphene coating makes carbon nanotube aerogels superelastic and resistant to fatigue. *Nat. Nanotechnol.* **7**, 562–566 (2012).
6. Olsson, R. T. et al. Making flexible magnetic aerogels and stiff magnetic nanopaper using cellulose nanofibrils as templates. *Nat. Nanotechnol.* **5**, 584–588 (2010).
7. Wu, M. M. et al. Superelastic graphene aerogel-based metamaterials. *Nat. Commun.* **13**, 4561 (2022).
8. Hu, H., Zhao, Z., Wan, W., Gogotsi, Y. & Qiu, J. Ultralight and highly compressible graphene aerogels. *Adv. Mater.* **15**, 2219–2223 (2013).
9. Xu, X. et al. Naturally dried graphene aerogels with superelasticity and tunable Poisson's ratio. *Adv. Mater.* **28**, 9223–9230 (2016).
10. Wang, X. et al. Scalable template synthesis of resorcinol-formaldehyde/graphene oxide composite aerogels with tunable densities and mechanical properties. *Angew. Chem.* **8**, 2397–2401 (2015).
11. Jiang, D. et al. Superelastic Ti_3C_2Tx MXene-based hybrid aerogels for compression-resilient devices. *ACS Nano* **15**, 5000–5010 (2021).
12. Li, C. et al. Temperature-invariant superelastic and fatigue resistant carbon nanofiber aerogels. *Adv. Mater.* **2**, 1904331 (2020).
13. Peng, M. et al. 3D printing of ultralight biomimetic hierarchical graphene materials with exceptional stiffness and resilience. *Adv. Mater.* **31**, 1902930 (2019).
14. Liu, Y., Shao, Z. & Vollrath, F. Relationships between super-contraction and mechanical properties of spider silk. *Nat. Mater.* **4**, 901–905 (2005).
15. Fu, Q. et al. Micro/nano multiscale reinforcing strategies toward extreme high-temperature applications: Take carbon/carbon composites and their coatings as the examples. *J. Mater. Sci. Technol.* **96**, 31–68 (2022).
16. Zhan, H. J. et al. Biomimetic carbon tube aerogel enables super-elasticity and thermal insulation. *Chem* **5**, 1871–1882 (2019).
17. Yang, M. et al. Biomimetic architected graphene aerogel with exceptional strength and resilience. *ACS Nano* **11**, 6817–6824 (2017).
18. Xu, X. et al. Double-negative-index ceramic aerogels for thermal superinsulation. *Science* **363**, 723–727 (2019).
19. Wang, Y. et al. Highly compressible and environmentally adaptive conductors with high-tortuosity interconnected cellular architecture. *Nat. Synth.* **1**, 975–986 (2022).
20. Zhu, H. X., Mills, N. J. & Knott, J. F. Analysis of the high strain compression of open-cell foams. *J. Mech. Phys. Solids* **45**, 1875–1904 (1997).
21. Cao, A., Dickrell, P. L., Sawyer, W. G., Ghasemi-Nejhad, M. N. & Ajayan, P. M. Super-compressible foamlike carbon nanotube films. *Science* **310**, 1307–1310 (2005).
22. Poncharal, P., Wang, Z. L., Ugarte, D. & De Heer, W. A. Electrostatic deflections and electromechanical resonances of carbon nanotubes. *Science* **283**, 1513–1516 (1999).
23. Yu, M. F. et al. Strength and breaking mechanism of multiwalled carbon nanotubes under tensile load. *Science* **287**, 637–640 (2000).
24. Xia, Z. H., Guduru, P. R. & Curtin, W. A. Enhancing mechanical properties of multiwall carbon nanotubes via sp^3 interwall bridging. *Phys. Rev. Lett.* **98**, 245501 (2007).
25. Kis, A., Jensen, K., Aloni, S., Mickelson, W. & Zettl, A. Interlayer forces and ultralow sliding friction in multiwalled carbon nanotubes. *Phys. Rev. Lett.* **97**, 025501 (2006).
26. Lu, D. et al. Lightweight and strong ceramic network with exceptional damage tolerance. *ACS Nano* **17**, 1166–1173 (2023).
27. Lu, D. et al. Scalable fabrication of resilient SiC nanowires aerogels with exceptional high-temperature stability. *ACS Appl. Mater. Interfaces* **11**, 45338–45344 (2019).
28. Vieira, J. M. & Brook, R. J. Kinetics of hot-pressing: the semilogarithmic law. *J. Am. Ceram. Soc.* **67**, 245–249 (1984).
29. Verhaverbeke, S. et al. The etching mechanisms of SiO_2 in hydrofluoric acid. *J. Electrochem. Soc.* **141**, 2852 (1994).
30. Lavini, F., Rejhon, M. & Riedo, E. Two-dimensional diamonds from sp^2 -to- sp^3 phase transitions. *Nat. Rev. Mater.* **7**, 814–832 (2022).
31. Yuan, G. et al. Proton-assisted growth of ultra-flat graphene films. *Nature* **577**, 204–208 (2020).
32. Bruley, J., Williams, D. B., Cuomo, J. J. & Pappas, D. P. Quantitative near-edge structure analysis of diamond-like carbon in the electron microscope using a two-window method. *J. Microsc.* **180**, 22–32 (1995).
33. Diociaiuti, M., Casciardi, S. & Sisto, R. The sp^2 and sp^3 fractions of unknown carbon materials: electron energy-loss near-edge structure analysis of CK spectra acquired under the magic-angle condition by the electron nanobeam technique. *Micron* **90**, 97–107 (2016).
34. Wu, Y. et al. Three-dimensionally bonded spongy graphene material with super compressive elasticity and near-zero Poisson's ratio. *Nat. Commun.* **6**, 1–9 (2015).
35. Qiu, L., Liu, J. Z., Chang, S. L., Wu, Y. & Li, D. Biomimetic superelastic graphene-based cellular monoliths. *Nat. Commun.* **3**, 1–7 (2012).
36. Liu, J. et al. Superelastic and multifunctional graphene-based aerogels by interfacial reinforcement with graphitized carbon at high temperatures. *Carbon* **132**, 95–103 (2018).
37. Pang, K. et al. Hydroplastic foaming of graphene aerogels and artificially intelligent tactile sensors. *Sci. Adv.* **6**, eabd4045 (2020).

38. Šilhavík, M. et al. Anomalous elasticity and damping in covalently cross-linked graphene aerogels. *Commun. Phys.* **5**, 27 (2022).
39. Li, C., Ding, M., Zhang, B., Qiao, X. & Liu, C. Graphene aerogels that withstand extreme compressive stress and strain. *Nanoscale* **10**, 18291–18299 (2018).
40. Li, X. H. et al. Vertically aligned, ultralight and highly compressive all-graphitized graphene aerogels for highly thermally conductive polymer composites. *Carbon* **140**, 624–633 (2018).
41. Gao, H. et al. Super-elastic and fatigue resistant carbon material with lamellar multi-arch microstructure. *Nat. Commun.* **7**, 1–8 (2016).
42. Si, Y. et al. Ultralight nanofibre-assembled cellular aerogels with superelasticity and multifunctionality. *Nat. Commun.* **5**, 1–9 (2014).
43. Guan, H., Cheng, Z. & Wang, X. Highly compressible wood sponges with a spring-like lamellar structure as effective and reusable oil absorbents. *ACS Nano* **12**, 10365–10373 (2018).
44. Chen, C. et al. Scalable and sustainable approach toward highly compressible, anisotropic, lamellar carbon sponge. *Chem* **4**, 544–554 (2018).
45. Chen, Z. et al. Wood-derived lightweight and elastic carbon aerogel for pressure sensing and energy storage. *Adv. Funct. Mater.* **30**, 1910292 (2020).
46. Wang, C. et al. Freeze-casting produces a graphene oxide aerogel with a radial and centrosymmetric structure. *ACS Nano* **12**, 5816–5825 (2018).
47. Liu, H. et al. Multifunctional superelastic, superhydrophilic, and ultralight nanocellulose-based composite carbon aerogels for compressive supercapacitor and strain sensor. *Adv. Funct. Mater.* **32**, 2113082 (2022).
48. Su, L. et al. Ultralight, recoverable, and high-temperature-resistant SiC nanowire aerogel. *ACS Nano* **12**, 3103–3111 (2018).
49. Zhang, X. et al. Ultrastrong, superelastic, and lamellar multiarch structured $\text{ZrO}_2\text{-Al}_2\text{O}_3$ nanofibrous aerogels with high-temperature resistance over 1300 °C. *ACS Nano* **14**, 15616–15625 (2020).
50. Zhang, X. et al. Three-dimensional reticulated, spongelike, resilient aerogels assembled by SiC/Si₃N₄ nanowires. *Nano. Lett.* **21**, 4167–4175 (2021).
51. Wang, H. et al. Ultralight, scalable, and high-temperature-resilient ceramic nanofiber sponges. *Sci. Adv.* **3**, e1603170 (2017).
52. Guo, J. et al. Hypocrystalline ceramic aerogels for thermal insulation at extreme conditions. *Nature* **606**, 909–916 (2022).
53. Thompson, A. et al. LAMMPS—a flexible simulation tool for particle-based materials modeling at the atomic, meso, and continuum scales. *Comput. Phys. Commun.* **271**, 108171 (2022).
54. Song, W. et al. Flexible graphene/polymer composite films in sandwich structures for effective electromagnetic interference shielding. *Carbon* **66**, 67–76 (2014).
55. Song, Q. et al. Carbon nanotube-multilayered graphene edge plane core-shell hybrid foams for ultrahigh-performance electromagnetic-interference shielding. *Adv. Mater.* **29**, 1701583 (2017).
56. Li, P. et al. Theoretical study and X-ray determination of bianthrone: Long C–C bond length and preferred gauche conformation. *J. Org. Chem.* **67**, 8002–8009 (2002).
57. Luo, C., Qi, X., Pan, C. & Yang, W. Diamond synthesis from carbon nanofibers at low temperature and low pressure. *Sci. Rep.* **5**, 1–6 (2015).
58. Côté, M. et al. Theoretical study of a three-dimensional all- sp^2 structure. *Phys. Rev. B* **58**, 664 (1998).
59. Stukowski, A. Visualization and analysis of atomistic simulation data with OVITO—the Open Visualization Tool. *Model. Simul. Mater. Sci. Eng.* **18**, 1–7 (2010).

Acknowledgements

The authors acknowledge the financial support from the Technical Field Foundation of China and National Natural Science Foundation of China (No. 52102077, 52072294, and 92263204). Additionally, the authors would like to thank the Instrument Analysis Center of Xi'an Jiaotong University for the assistance with TEM, XPS, and Raman tests, as well as W.L., T.Y.L., and H.Y.N. at Northwestern Polytechnical University for the help with high-temperature annealing and EMI shielding tests.

Author contributions

L.Z. and H.J.W. conceived and designed the research. L.Z., D.L., and J.J.Z. participated in materials preparation and mechanical tests. L.Z. wrote the paper. H.J.W. supervised the research. Y.B.Q. and P.Z. carried out the in situ TEM characterization. P.F.G., L.S., X.L., M.N., and K.P. discussed the results and analyzed the data.

Competing interests

The authors declare no competing interests.

Additional information

Supplementary information The online version contains supplementary material available at <https://doi.org/10.1038/s41467-023-38664-6>.

Correspondence and requests for materials should be addressed to Hongjie Wang.

Peer review information *Nature Communications* thanks Jiri Cervenka and the other, anonymous, reviewer(s) for their contribution to the peer review of this work. A peer review file is available.

Reprints and permissions information is available at <http://www.nature.com/reprints>

Publisher's note Springer Nature remains neutral with regard to jurisdictional claims in published maps and institutional affiliations.

Open Access This article is licensed under a Creative Commons Attribution 4.0 International License, which permits use, sharing, adaptation, distribution and reproduction in any medium or format, as long as you give appropriate credit to the original author(s) and the source, provide a link to the Creative Commons license, and indicate if changes were made. The images or other third party material in this article are included in the article's Creative Commons license, unless indicated otherwise in a credit line to the material. If material is not included in the article's Creative Commons license and your intended use is not permitted by statutory regulation or exceeds the permitted use, you will need to obtain permission directly from the copyright holder. To view a copy of this license, visit <http://creativecommons.org/licenses/by/4.0/>.

© The Author(s) 2023